PERGAMON

Journal of the Mechanics and Physics of Solids
51 (2003) 607–635

JOURNAL OF THE
MECHANICS AND
PHYSICS OF SOLIDS

www.elsevier.com/locate/jmps

# An examination of the competition between bulk behavior and interfacial behavior of ceramics subjected to dynamic pressure–shear loading

P.D. Zavattieri[1], H.D. Espinosa*

*Department of Mechanical Engineering, Northwestern University, 2145 Sheridan Road, Evanston, IL 60208-3111, USA*

Received 9 August 2001; accepted 16 September 2002

**Abstract**

A grain level micromechanical analysis of ceramic microstructures subjected to dynamic compression–shear loading conditions is presented. The investigation consists of a combined experimental/numerical approach in which bulk and surface properties are examined by means of pressure–shear impact experiments for a ceramic plate in contact with steel plates. The model for the ceramic microstructure accounts for heterogeneities and randomness in grain orientation and composition. A cohesive zone model is included to capture inter-granular microcrack initiation and evolution as a natural outcome of the calculated material response. Surface roughness is also included in the analysis to capture the time-dependent frictional behavior of the various interfaces. The model for the steel anvil plate accounts for visco-plasticity, thermal softening and strain hardening. Representative volume elements of ceramic microstructure and anvil plates are considered to account for features observed in real experiments. Pressure–shear impact velocity histories are used not only to identify inelasticity, but also to determine dominant failure modes. Bridging between micro- and macroscales is achieved by using the developed model. Simulated velocity histories have been found to be in a good agreement with the experimental observations when bulk and surface features are included in the analysis. However, it is demonstrated that information gathered from these experiments is not sufficient to determine the mechanical behavior of the brittle material. Instead, the velocity histories provide important information on the time-dependent frictional behavior of the specimen–anvil interfaces.


*Keywords:* Tribology; Ceramics; Dynamic friction; Damage

* Corresponding author. Tel.: +1-847-467-5989; fax: +1-847-491-3915.
*E-mail address:* espinosa@northwestern.edu (H.D. Espinosa).
*URL:* http://www.mech.northwestern.edu/espinosa

[1] Current address. General Motors Research & Development Center, 30500 Mound Road, Warren, MI 48090-9055, USA.

0022-5096/03/$ - see front matter 
PII: S0022-5096(02)00103-5

## 1. Introduction

Critical elements in the development of a physically based model of the dynamic deformation and failure of ceramics require experiments specifically designed to examine inelasticity. For instance, an experiment that can generate controlled microcracking, under well-defined stress histories, was developed by Clifton and co-workers, to study the initiation and evolution of microcracks in ceramics, see, Raiser et al. (1990), Espinosa et al. (1992), Espinosa (1992), Raiser et al. (1994), Raiser (1993), and Espinosa and Nemat-Nasser (2000). These investigators performed plate impact *soft recovery* experiments by subjecting the central region of a square ceramic specimen to known and controllable stress pulses. Microcracking resulted, yet the specimens were recovered intact for microscopic analysis and comparison with numerical simulations. A grain level analysis of these experiments for the case of alumina is given in Zavattieri and Espinosa (2001). More recently, these recovery experiments were extended to *pressure–shear* by Espinosa (1992), Yadav et al. (1993), Machcha and Nemat-Nasser (1994), Espinosa et al. (1997), and Espinosa et al. (2000b), to provide combined pressure and shear loading. The objective is to study the dynamic shearing resistance of materials and dynamic friction (Espinosa et al., 1997).

Pressure–shear experiments offer unique capabilities for the characterization of advanced materials under dynamic loading conditions. These experiments allow high stresses, high pressures, high strain rates and finite deformations to be generated under well-characterized conditions. All the experiments rely on the generation of one-dimensional waves in the central region of the specimen in order to allow a clear interpretation of the experimental results and the mathematical modeling of the material behavior. Compression–shear loading is attained by inclining the flyer, specimen, and target plates with respect to the axis of the projectile, e.g., Clifton and Klopp (1985). By varying the angle of inclination, a variety of loading states may be achieved.

Pressure–shear *soft recovery* experiments offer several advantages over other experimental techniques in the study of damage and inelasticity in advanced materials (Espinosa et al., 2000b). The stress amplitudes and deformation rates generated in these experiments allow the identification of damage and material instabilities (Zhou et al., 1994). One advantage of these experiments is that they allow the constitutive relation between shear stress, shear strain and shear strain rate to be obtained directly according to the one-dimensional elastic wave theory (Clifton and Klopp, 1985) as long as frictional sliding between specimen, flyer and target plates does not occur. The one-dimensional elastic wave theory can be used to construct $\tau$–$\gamma$ curves at strain rates as high as $1 \times 10^6\ \mathrm{s}^{-1}$ and pressures in the range of 2–5 GPa.

Ideally, the information gathered from these experiments can be substantially increased by correlation of real-time velocity profiles and microstructural features associated with mechanisms of inelasticity and damage observed on recovered samples. Espinosa et al. (2000b) and Zavattieri et al. (2001) have shown that irrespective of how efficient the wave release is, microcracks further grow and coalesce during unloading resulting in material fragmentation. Ceramics are so susceptible to fragmentation that they can pulverize upon unloading if enough damage and elastic energy is stored within the material in the loading phase. Due to the impossibility of

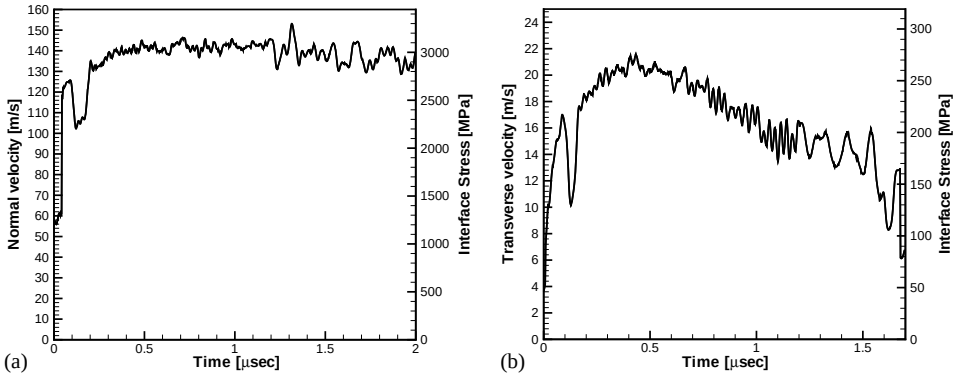


Fig. 1. (a) Normal velocity history from pressure–shear experiment 7-1025 (Espinosa et al., 2000b). The plotted time is after arrival of normal wave to anvil back surface. (b) Transverse velocity history from the same experiment.

recovering intact brittle materials, when stresses high enough to initiate damage are applied, interpretation of failure mechanisms and their kinetics require numerical simulation of the experiments.

A typical velocity history obtained in pressure–shear *soft recovery* experiments is shown in Fig. 1. The normal velocity–time profile obtained from experiment 7-1025, see Espinosa et al. (2000b), is shown in Fig. 1(a). The normal particle velocity shows a velocity reduction after an initial jump indicating the presence of a small gap between the $Al_2O_3/SiC$ nanocomposite and the multi-plate flyer. Upon reverberation of waves within the specimen, the normal velocity rises to a value of about 140 m/s, at approximately 0.4 μs and remains almost constant until release waves from the boundary reach the observation point. The peak normal stress in this shot, based on one-dimensional wave theory (Clifton and Klopp, 1985), ($\sigma = \rho c_1 u_{fs}/2$), reaches 3.45 GPa. The transverse particle velocity history for the same experiment is shown in Fig. 1(b). The velocity rises progressively and then drops for a few nanoseconds. Since in this experiment shear motion is transferred by friction, a reduction in normal traction at the specimen–flyer plate interface, results in a drop of the transmitted shear motion. When the gap closes, the transverse velocity increases until it reaches a maximum value of 22 m/s at about 500 ns. Then it decays continuously while the normal velocity remains constant, see Figs. 1(a) and (b). The maximum shear stress, given by one-dimensional wave theory (Clifton and Klopp, 1985), as $\tau = \rho c_2 v_{fs}/2$, is 280 MPa. This value is well below the expected shear stress of 575 MPa assuming elastic material response. As previously mentioned, the observed transverse velocity histories could be the result of frictional damage and/or bulk material damage.

At present, full numerical simulations at the grain size level with models accounting for grain boundary fracture, grain plasticity and interface contact, seem to be the only avenue to identify failure modes of brittle materials. The calculation requires the modeling of flyer and target (*anvil*) plates, including roughness of the surfaces in contact and various material inelasticity mechanisms. Calculation of stress and strain distributions

in real microstructures increases our understanding of different inelastic mechanisms controlling macroscopic response. Furthermore, these micromechanical simulations are useful for quantification and determination of dominant failure mechanisms, as well as the derivation of evolution equations to be used in continuum and discrete models (Curran et al., 1990; Espinosa, 1995; Espinosa et al., 1998a). In this way, bridging between length scales is accomplished.

Within this framework, a micromechanical model has been proposed by Zavattieri et al. (2001) to assess intergranular microcrack initiation and evolution in brittle materials. A two-dimensional plane strain representative volume element (RVE) of an actual microstructure, subjected to multi-axial dynamic loading, is considered for the analyses. Assuming that the only source of non-linearity is given by inter-granular microcracking, a large deformation elastic–anisotropic model for the grains, incorporating grain anisotropy by randomly generating principal material directions, is included. Cohesive interface elements are embedded along grain boundaries to simulate microcrack initiation and evolution. Their interaction and coalescence are a natural outcome of the calculated material response. With this micromechanical model, they analyzed the effect of the inelastic material parameters of the ceramic on the velocity history obtained by Espinosa et al. (2000b). It was observed that the velocity profiles at the bottom face of the specimen do not change significantly even when the level of ceramic damage varies significantly. Even though in their simulations the evolution of crack density and pattern changes from an almost intact ceramic to a completely cracked ceramic, the changes in the normal and transverse velocity do not reproduce the measured velocity histories. In their simulations, the presence of the target and flyer has been only taken into account as viscous non-radiating interfaces. Contact and sliding between the specimen and anvils have not been considered.

The objective of this work is to improve the model proposed by Espinosa and co-workers, see Zavattieri et al. (2001) and Espinosa and Zavattieri (2002a, b), such that contact and frictional sliding are explicitly included in the model. Surface roughness is accounted for in the analysis by introducing irregularities in the contact surfaces of the specimen and anvil plates directly in the initial finite element model. The unique advantages of the micromechanical model proposed in this work include: (1) explicit account of real and arbitrary material microstructures, (2) explicit modeling of fracture in a non-constrained manner, therefore arbitrary crack paths or microcrack patterns are admitted, (3) direct analysis of the stochastic nature of fracture in heterogeneous microstructures, (4) consideration of the effect of residual stresses, (5) resolution of fracture over multiple length scales without limitations imposed by “ad hoc” fracture criteria; therefore, crack initiation, growth, coalescence and interaction are a natural outcome of material response, applied loading, and boundary constraints, (6) the representative computational cells where the calculations take place are chosen such that direct comparison with experimental data can be made, (7) surface roughness can be included explicitly in the finite element mesh for the analysis of contact and sliding between the specimen and anvil plates.

The implementation of an iterative computational/experimental procedure seems promising, since experiments provide limited quantitative information on crack density, their rate of change as a function of applied deformation rate, and friction properties.

The objective of this work is to provide tools and means to understand the macroscopic bulk and surface response of brittle materials when subjected to dynamic multi-axial loading at the micron scale.

## 2. Numerical approach

### 2.1. Micromechanical model

The finite element analysis of the initial boundary value problem is performed using a total Lagrangian continuum approach with a large deformation elastic and thermo-elastic visco-plastic model (Zavattieri et al., 2001; Espinosa and Zavattieri, 2002a). An anisotropic thermo-elastic model is used to describe the single crystal anisotropic behavior of grains. The second Piola–Kirchhoff stress tensor relative to the undeformed configuration is described by $\mathbf{S}_{ij} = \mathscr{C}_{ijkl}\mathbf{H}_{kl}$, where $\mathbf{H}$ is a logarithmic strain measure or Hencky strain, and $\mathscr{C}_{ijkl}$ is the elastic anisotropic material stiffness tensor in the global co-ordinates. Each grain is assumed to be elastic–orthotropic and the orientation of the principal material directions differs from grain to grain. In order to keep the plane strain condition in the $x$–$y$ plane, one of the principal material directions, which is chosen randomly, must coincide with the $z$-axis. The angle between the global axes $x$, $y$, and the two local axes lying in the plane $x$–$y$ is also generated randomly. In general, this approach could be used for any orthotropic material where the normal to the three symmetry planes coincides with the local axes of co-ordinates, i.e. tetragonal systems: *Indium*, *Tin*, *Zircon*; transversely isotropic systems: *Cadmium*, *Ice*, *Zinc*; cubic: *Aluminum*, *Copper*, *Nickel*, *etc*.

A multi-body contact-interface algorithm is used to describe the kinematics at grain boundaries and to simulate crack initiation and propagation. Fig. 2 describes the contact model, which is integrated with interface elements to simulate microcracking at grain boundaries and subsequent large sliding, opening and closing of the interface. The tensile and shear tractions in the zero thickness interface elements, embedded along grain boundaries, are calculated from the interface cohesive law. The interface cohesive law describes the evolution of these tractions in terms of both normal and tangential displacement jumps. Within the framework of cohesive interface elements, the two most noteworthy cohesive failure models available in the literature are the potential-based law (Tvergaard, 1990; Xu and Needleman, 1995; Espinosa et al., 1998b) and the linear law (Camacho and Ortiz, 1996b; Espinosa et al., 1998a; Ortiz and Pandolfi, 1999; and Zavattieri et al., 2001).

The model assumes that the interface carries forces that oppose separation and shear between the surfaces until debonding. The magnitude of these forces is a function of the relative separation and shear displacements between the two surfaces. In formulating the cohesive law, a non-dimensional effective displacement jump is defined by $\lambda_{\mathrm{d}} = \sqrt{(u_{\mathrm{n}}/\delta_{\mathrm{n}})^2 + \xi^2(u_{\mathrm{t}}/\delta_{\mathrm{t}})^2}$, where, $u_{\mathrm{n}}$ and $u_{\mathrm{t}}$ are the actual normal and tangential displacement jumps at the interface estimated by the finite element analysis, and $\delta_{\mathrm{n}}$ and $\delta_{\mathrm{t}}$ are critical values at which interface failure takes place. For a triangular $T - \lambda_{\mathrm{d}}$ law, see Fig. 2, the normal and tangential components of the traction vector, in the

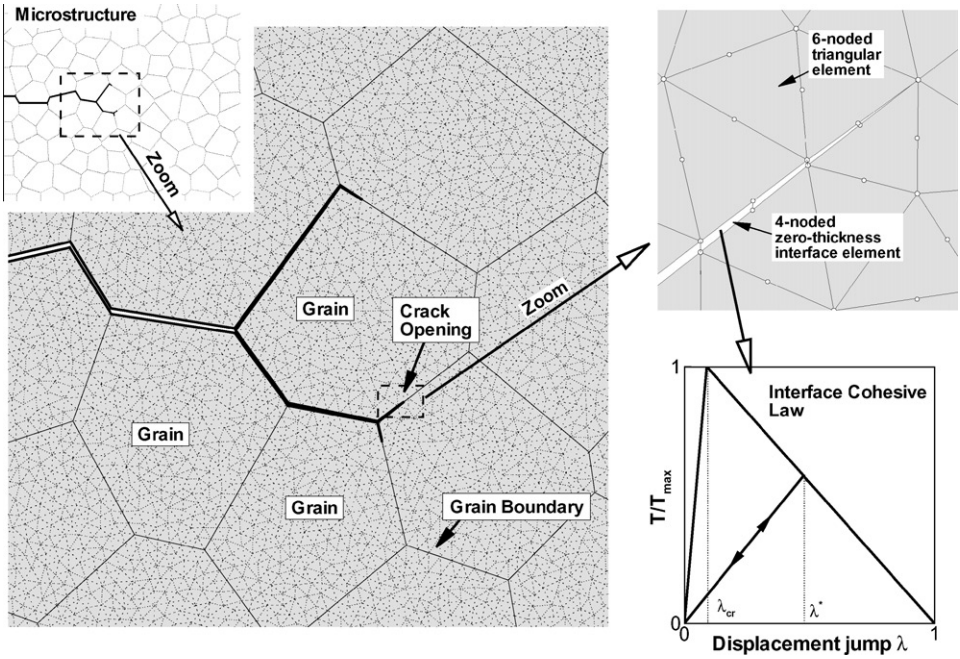


Fig. 2. Schematics of microcracking at grain boundaries using an irreversible interface cohesive law. Evolution of traction with loading and unloading is shown.

range $0 \leqslant \lambda_d \leqslant \lambda_{cr}$, are given by

$$T_n = \frac{u_n}{\delta_n}\frac{T_{max}}{\lambda_{cr}}, \qquad T_t = \alpha\frac{u_t}{\delta_t}\frac{T_{max}}{\lambda_{cr}}, \tag{1}$$

and for loading in the range $\lambda_{cr} < \lambda_d \leqslant 1$,

$$T_n = T_{max}\frac{u_n}{\delta_n}\frac{1-\lambda_d}{\lambda_d(1-\lambda_{cr})}, \qquad T_t = \alpha T_{max}\frac{u_t}{\delta_t}\frac{1-\lambda_d}{\lambda_d(1-\lambda_{cr})}. \tag{2}$$

$T_{max}$ is the maximum normal traction that the interface can develop before failure and $\alpha = \xi^2(\delta_n/\delta_t)$ is the parameter coupling the normal and shear tractions, such that $\xi^2 = G_{IIC}/G_{IC}$.

It is assumed here that the traction can increase reversibly and linearly to its maximum value $T = T_{max}$ when $\lambda_d = \lambda_{cr}$. Beyond $\lambda_{cr}$, the traction reduces to zero up to $\lambda_d = 1.0$ and any unloading takes place irreversibly (Zavattieri et al., 2001; Espinosa and Zavattieri, 2002a), which means that the interface between bodies is intact until the interface traction reaches the maximum value $T_{max}$. Once the maximum traction is reached, the interface starts failing and the traction reduces to zero linearly up to the maximum displacement jump. From the values of fracture toughness $K_{IC}$, or equivalently $G_{IC}$, assuming plane strain, and the maximum interface stress, the critical interface displacement jump is computed by equating the area under the $T-\delta$ diagram to $G_{IC}$. The compressive tractions at the grain boundaries are calculated either with

the compressive part of the $T-\delta$ relationship or with the impenetrability condition employed in the contact model, depending on whether there are large displacements. More detail on this cohesive interface model can be found in Espinosa et al. (2000a), Zavattieri et al. (2001), and Espinosa and Zavattieri (2002a).

The initial slope of the tension/compression cohesive law was selected specially to prevent the addition of cohesive elements from changing the speed at which longitudinal and shear waves propagate in the material. For a detailed discussion of these and other numerical features of the implemented cohesive laws, see Zavattieri and Espinosa (2001).

### 2.2. Large deformation plasticity model for the anvil plates

The plasticity constitutive law used in this analysis is based on an atomic lattice model for metals to describe elastic and plastic material behavior (Camacho and Ortiz, 1996a; Espinosa et al., 1998b). The total deformation gradient field $\mathbf{F}$ is the result of two main mechanisms of deformation: (1) dislocation motion within the active slip systems of the crystal, and (2) lattice distortion $\mathbf{F}=\mathbf{F}^{\mathrm{e}}\mathbf{F}^{\mathrm{p}}$. Within a J2-flow formulation, the plastic flow direction is a function of the deviatoric part of the second Piola–Kirchhoff stress tensor, $\bar{\mathbf{S}}_{\mathrm{dev}}$ in the intermediate configuration $\bar{\mathbf{N}}=3\bar{\mathbf{S}}_{\mathrm{dev}}/(2\bar{\sigma})$. The effective plastic strain rate, $\dot{\varepsilon}^{\mathrm{p}}$, is a function of the effective stress $\bar{\sigma}$, temperature $T$, and the internal variables. For a visco-plastic model, a common representation of this function is,

$$\dot{\varepsilon}^{\mathrm{p}}=\dot{\varepsilon}_0^{\mathrm{p}}\left[\left(\frac{\bar{\sigma}}{s(\varepsilon^{\mathrm{p}},T)}\right)^{\alpha_{\mathrm{r}}}-1\right]\quad \text{if } \bar{\sigma}>\mathbf{s}, \tag{3}$$

$$\dot{\varepsilon}^{\mathrm{p}}=0\quad \text{if } \bar{\sigma}\leqslant\mathbf{s}, \tag{4}$$

$$s(\varepsilon^{\mathrm{p}},T)=\sigma_0\left(1+\frac{\varepsilon^{\mathrm{p}}}{\varepsilon_0^{\mathrm{p}}}\right)^{1/\beta}\left[1-\left(\frac{T-T_0}{T_{\mathrm{m}}-T_0}\right)^{\gamma}\right], \tag{5}$$

such that $\varepsilon^{\mathrm{p}}$ is the accumulated plastic strain, $\sigma_0$ is the initial yield stress, $T_{\mathrm{m}}$ is the melting temperature of the material, $T_0$ is the reference temperature, and $\alpha_{\mathrm{r}}$, $\beta$, and $\gamma$ are the rate sensitivity, hardening, and thermal softening exponents.

Large plastic strains and strain rates result in temperature increases in the body. Therefore, a temperature-dependent material model and heat conduction need to be added to account for the fact that the behavior of most materials can change dramatically as the temperature rises. The rise in temperature is usually caused by the generation of heat through plastic deformation. In this analysis, heat production and transfer are controlled by $k\nabla^2T+Q=c\rho\dot{T}$ in volume $B_t$, where $Q$ is the heat source, $\rho$ is the mass density, $c$ is the specific heat, and $k$ is the thermal conductivity. For the plastic process, a heat supply $Q$ due to the rate of plastic work, $\dot{W}^{\mathrm{p}}$, can be estimated by the Taylor–Quinny formula, viz., $Q=\delta\dot{W}^{\mathrm{p}}$, in which $\delta$ is a coefficient of the order of 0.8–0.9. A more detailed description of the algorithm can be found in Espinosa et al. (1998b).

### 2.2.1. Adaptive remeshing

In the presence of large deformations, such as the one in the flyer and target steel plates near the contact surfaces, the mesh becomes distorted, errors accumulate and the time step required by the explicit integration algorithm tends to dwindle such that completing a dynamic calculation may become extremely expensive from a computational viewpoint. In this work a novel and versatile refinement/coarsening technique developed by Espinosa et al. (1998b, 2001) is used. This technique consists mainly in an optimization problem where the aim is to improve the quality of the mesh by performing certain operations over the mesh. Unlike automatic mesh generators, optimization uses the information of the old mesh to construct the new one. This procedure has been demonstrated to be most efficient and straightforward way to increase the efficiency of the finite element results.

The objective function, which is the quality of the mesh, contains the information of the size and shape of the element according to refinement and coarsening criteria. The quality of the mesh $\tau$ can be described by the following expression:

$$Q_\tau = \min Q_k, \quad k \in \tau, \tag{6}$$

where $Q_k$ is element quality, which is defined by

$$Q_k = Q_{\text{shape}}\, Q_{\text{size}}$$

where

$$Q_{\text{shape}} = \mathbf{C} V_k / P_k^d;$$

$$Q_{\text{size}} = \exp[-\eta^2 \log^2(h_k/h^*)]. \tag{7}$$

$Q_{\text{shape}}$ is the "*shape*" quality of the element. In two-dimensional $d=2$, $\mathbf{C}=20.78$, $V_k$ is the area of the element and $P_k$ is the perimeter. This quality has been proposed by Zavattieri et al. (1996a, b) and only accounts for shape distortions. $Q_{\text{shape}}$ varies from 0 for a totally collapsed element to 1 for an equilateral triangle. The "*size*" quality $Q_{\text{size}}$ proposed by Buscaglia and Dari (1997) and Buscaglia et al. (1997) takes into account the size of the element $h_k$. Given the desired element size $h^*$ this quality can go from 0, when $h_k \ll h_k^*$ or $h_k \gg h_k^*$, to 1 when $h_k = h_k^*$. This is a log-Gaussian function centered at $h_k = h^*$. The parameter $\eta$ determines the width of the *size* quality; for two dimensional, Buscaglia et al. (1997) have successfully taken $\eta = 0.7$, meaning that an equilateral triangle with edge size half or twice the desired one has a quality $e^{-1} = 0.368$. For our calculations the element size is taken as $h_k = P_k/3$. It is useful to introduce more elements in those regions of the mesh that are rapidly deforming. This decision is based on the rate of plastic work, $\dot{W}^{\text{p}} = \sigma\dot{\varepsilon}^{\text{p}}$, and $h_k^*$ is calculated according to this quantity. A summary of this procedure is given in Espinosa et al. (2001).

The global algorithm consists basically of two parts: the *topological* and *geometrical* optimization. In the topological optimization, the submesh formed by $\bar{k}$ and its neighbors (elements sharing a node or an edge with $\bar{k}$) is considered. Several operations are *virtually* performed on this submesh, until one is found that yields a better quality. This operation is then *really* performed (Buscaglia and Dari, 1997). The operations consist in defining a *cluster*, removing its interior node, and either connecting all the

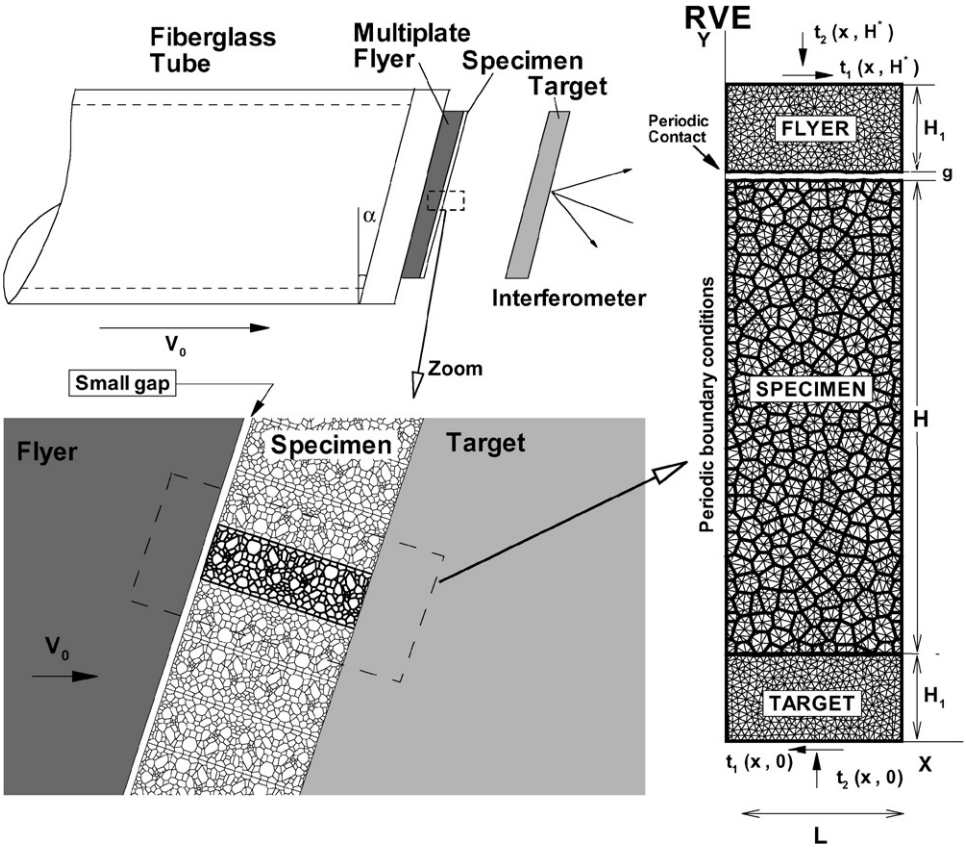


Fig. 3. Schematics of experimental configuration and representative volume element.

edges in the cluster boundary to one of the boundary nodes or connecting them to a node at the center of the cluster. Two types of clusters are considered, *edge* clusters are all elements that share a given edge, and *nodal* clusters are all elements that share a given node.

Although this topological mesh optimization improves the shape of the elements, it does not allow the nodes to move, and it is highly possible that some elements will end up highly deformed. The node-movement optimization algorithm (also called *geometrical* mesh optimization) proposed by Zavattieri et al. (1996b) is used. Details on the *mesh transfer operator* utilized in this work is given in Espinosa et al. (1998b).

### 2.3. Boundary conditions

Pressure–shear simulations are performed taking into account the contact between flyer, target and specimen plates. Fig. 3 shows the pressure–shear configuration used in experiment 7-1025 performed by Espinosa et al. (2000b). Unlike simulations presented

Table 1
Material properties for the specimen

| Anisotropic elastic constant for alumina $Al_2O_3$ | Hearmon (1956) (GPa) |
|---|---|
| $C_{11} = C_{22}$ | 465 |
| $C_{12}$ | 124 |
| $C_{13} = C_{23}$ | 117 |
| $C_{33}$ | 563 |
| $C_{44} = \frac{1}{2}(C_{11} - C_{12})$ | |
| $C_{55} = C_{66}$ | 233 |

in previous works, in these simulations the specimen of thickness $H$ is attached to the flyer and its initial velocity is the same as the flyer initial velocity, i.e., $V_0 =$ 148 m/s. The angle of inclination in this case is $\alpha = 18°$. The specimen–flyer interface possesses a gap of magnitude $g$. This gap results from the assembly of the plates, see Espinosa et al. (2000b), for details.

Assuming that the computational cell is repeated in the $x$ direction, the following periodic boundary conditions are applied $\mathbf{u}(0, y, t) = \mathbf{u}(L, y, t)$, $\mathbf{v}(0, y, t) = \mathbf{v}(L, y, t)$, $\mathbf{a}(0, y, t) = \mathbf{a}(L, y, t)$, where $\mathbf{u}$, $\mathbf{v}$ and $\mathbf{a}$ are the displacement, velocity and acceleration vector fields. Grains with nodes at $x = 0$ have the same principal material directions as the grains with nodes at $x = L$ in order to ensure periodicity.

Furthermore, assuming that flyer and target plates remain elastic, except for a thin layer at the flyer–specimen and specimen–target interfaces, computational effort can be minimized by replacing the rest of the flyer and anvil plates by a layer of thickness $H_1$ with viscous boundary conditions obtained from one-dimensional elastic wave theory.

Conservation of momentum and continuity of velocities and tractions lead to the following equations for tractions $t_x$ and $t_y$ at the back of the momentum trap and at the front of the flyer.

$$t_x(x, H^*, t) = (\rho c_s)_f [v_x(x, H^*, t) - v_x^0], \tag{8}$$

$$t_y(x, H^*, t) = (\rho c_l)_f [v_y(x, H^*, t) - v_y^0], \tag{9}$$

$$t_x(x, 0, t) = (\rho c_s)_t v_x(x, 0, t), \tag{10}$$

$$t_y(x, 0, t) = (\rho c_l)_t v_y(x, 0, t), \tag{11}$$

where $(\ )_f$ and $(\ )_t$ denote flyer and target quantities, $c_l$ and $c_s$ are longitudinal and shear wave speeds, $\rho$ is the specific material density, $v_x$ and $v_y$ are in-plane and normal velocities, $v_x^0$ and $v_y^0$ are the in-plane and normal velocities of the flyer plate and $H^* = H + 2H_1 + g$. The flyer shear and normal velocities are obtained from the projectile velocity, $V_0$ and pressure shear angle $\alpha$ as $v_x^0 = V_0 \sin\alpha$, $v_y^0 = V_0 \cos\alpha$. The initial in-plane and normal velocities at the back of the target are zero and at the front of the flyer they are given by $v_x(x, H^*, 0) = v_x^0$ and $v_y(x, H^*, 0) = v_y^0$.

The material properties of the ceramic specimen are given in Table 1. For simplicity, the non-zero components of the constitutive law are denoted by only two indices (i.e.

Table 2
Mechanical material properties for the anvil plates

| Flyer/target properties | Hampden steel |
|---|---|
| *Elastic properties* | |
| Young's modulus $E$ | 214.3 GPa |
| Poisson's ratio $\nu$ | 0.299 |
| Density $\rho$ | 7861 kg/m$^3$ |
| Longitudinal wavespeed $C_l$ | 6057 m/s |
| Shear wavespeed $C_s$ | 3238 m/s |
| Longitudinal impedance $(\rho C_l)_s$ | 47.62 GPa/mm/μsec |
| Shear impedance $(\rho C_s)_s$ | 25.46 GPa/mm/μsec |
| *Inelastic properties* | |
| Initial yield stress $\sigma_0$ | 1 GPa |
| Reference plastic strain $\varepsilon_0^p$ | 0.026 |
| Reference plastic strain rate $\dot{\varepsilon}_0^p$ | 1000 s$^{-1}$ |
| Rate sensitivity exponent $\alpha_r$ | 3 |
| Hardening exponent $\beta$ | 1000 |

Table 3
Thermal material properties

| | Alumina ($Al_2O_3$) | Hampden steel |
|---|---|---|
| Specific heat $c$ (J/kg/K) | 795 | 477 |
| Thermal conductivity $k$ (W/m/K) | 26 | 38 |
| Taylor–Quinny coeff. $\delta$ | 0.9 | 0.9 |
| Reference temperature $T_0$ (°K) | 293 | 293 |
| Melting temperature $T_m$ | 2323 | 1700 |
| Thermal softening exponent $\gamma$ | 1 | 0.5 |

$C_{1111}=C_{11}$, $C_{2222}=C_{22}$, etc). It should be noted that the behavior of alumina is assumed to be transversely isotropic (or hexagonal), while the real crystal structure is known to be a trigonal system (in which only one angle can vary). A detailed explanation of why this assumption does not affect the numerical analysis is given in Zavattieri et al. (2001).

The elastic and inelastic material properties for flyer and target (*anvil*) plates are given in Table 2. Since the thermo-mechanical coupling, described in Section 2.2, is considered in the analysis to asses the frictional sliding between the bodies, the thermal properties for both materials are given in Table 3.

### 2.4. Contact and frictional sliding

As discussed previously, the consideration of target and flyer plates in the simulations introduces a new complexity in the analyses. A versatile multi-body contact model for explicit dynamic analysis is used for this study to account for the contact and

frictional sliding between the specimen and anvil plates. This algorithm is based on predicting accelerations assuming no contact, and later correcting the accelerations of the surface nodes so that the surfaces do not interpenetrate (Taylor and Flanagan, 1987). This surface-based contact algorithm allows contact between bodies that undergo large relative displacements as they move. The contact algorithm presumes that one body is the master and the other is the slave, where a segment of the master body is penetrated by a node of the slave. A detailed description of this algorithm can be found in Espinosa et al. (1998b).

Furthermore, the contact algorithm has been extended to take into account the periodic nature of the boundary conditions in the RVE. If there is sliding and periodicity that is not accounted for in the contact, the specimen could exhibit false contact and even lose contact with the flyer and target. To circumvent this problem, the multi-body contact algorithm has been modified to consider periodicity when sliding is present. The algorithm takes into account the contact in the borders of the representative volume element as indicated in Fig. 4(a).

### 2.4.1. Surface roughness parameters

In general, surface roughness is highly complex because many surface finishing processes, such as polishing, grinding, and shot blasting are stochastic by nature. There is a great variety of surface parameters, many of which have been developed to characterize the function describing engineering surfaces for particular applications. The most common statistical descriptors of surface height are the roughness average, $R_a$, and the root mean square (RMS) roughness (also called $R_q$). These are closely related and are given by the following equations, shown in integral and discrete forms:

$$R_a = \frac{1}{L}\int_0^L \|y(x)\|\,dx = \frac{1}{N}\sum_{i=1}^{N}\|y_i\|, \tag{12}$$

$$\mathrm{RMS} = \left[\frac{1}{L}\int_0^L y^2(x)\,dx\right]^{1/2} = \left[\frac{1}{N}\sum_{i=1}^{N} y_i^2\right]^{1/2}, \tag{13}$$

where $y(x)$ is the surface profile, sampled by the set of $N$ points, $y_i$, over the length, $L$. The parameters $R_a$ and RMS are useful estimators of the average heights and depths of surface profiles. The RMS roughness is commonly specified for surfaces of optical components.

In addition to these two averaging height parameters, an assortment of other parameters has been defined; such as wavelength parameters, which are used to characterize the spacing between peaks and valleys of the surface profile. The wavelength parameter is often characteristic of the process that formed the surface and the material. A typical wavelength parameter is the mean peak spacing $\lambda$, defined for a surface profile as the

Fig. 4. (a) Schematics of periodicity in the contact when the specimen slides over the target. (b) Finite element mesh utilized for the pressure–shear simulations. Detail of roughness profiles corresponding to the various contact surfaces. The $R_a$ value was obtained from experimental measurements.

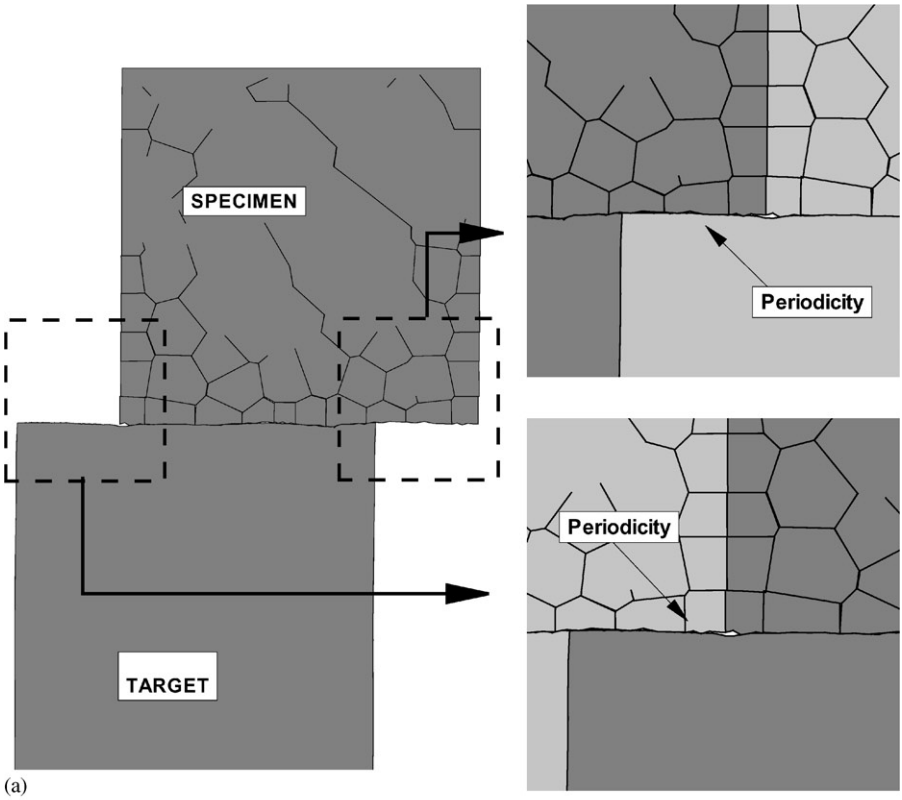
SPECIMEN
TARGET
Periodicity
Periodicity

(a)

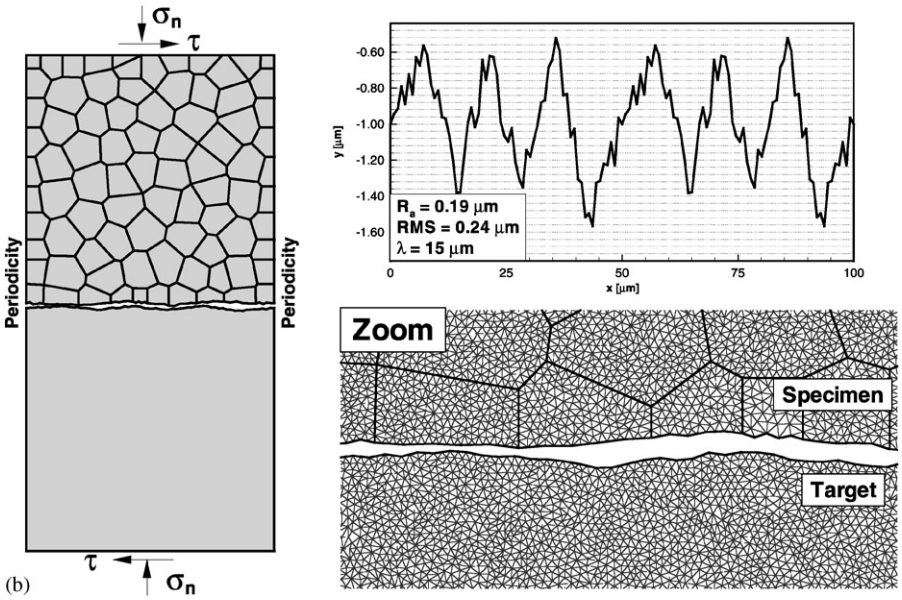
σn
τ
Periodicity
Periodicity
τ
σn
-0.60
-0.80
-1.00
-1.20
-1.40
-1.60
y [μm]
0
25
50
75
100
x [μm]
Ra = 0.19 μm
RMS = 0.24 μm
λ = 15 μm
Zoom
Specimen
Target

(b)

average spacing between two successive peaks. In the simulations discussed later, these two parameters are used to describe the surfaces in contact.

## 3. Analysis of frictional sliding between specimen and target plates

Universal agreement of what truly causes friction does not exist. It is clear, however, that friction is due to a number of mechanisms that probably act together but that may appear in different proportions under different circumstances. The word "*friction*" is used to describe the gradual loss of kinetic energy in many situations where bodies or substances move relative to one another.

In order to conduct a preliminary study of frictional sliding between specimen and steel target, the computational cell considered in the simulations includes only a small portion of the ceramic and target instead of the whole thickness of the ceramic. The dimensions of the specimen and target are $50 \times 50$ μm. Fig. 4(b) shows the finite element mesh utilized in this analysis. Full-scale simulations are reported in a later section.

The values of $R_a$ and RMS have been taken from previous experimental measurements (Espinosa et al., 2000b). The amplitude between the peaks and valleys is 1.2 μm, and according to these experimental measurements the wavelength is $\lambda \approx 15$ μm. Fig. 4(b) also shows a detail of the specimen–flyer and specimen–target interfaces along with roughness characteristics of the various surfaces. The boundary conditions applied in this computational cell are similar to Eqs. (8)–(11), except that the tractions $t_x$ and $t_y$ applied at the top of the ceramic representative volume element are given by the impedance of the ceramic.

To consider this micromechanical model valid, the response of the material should not depend on numerical parameters, such as element size and size of the representative volume element in consideration. The width of the representative volume element is chosen such that at least two or three peaks and valleys are included, while periodicity is enforced. The height is chosen such that the condition of uniform displacement and velocities on top and bottom of the RVE is not violated. Since cylindrical waves are generated at contact points, the average distance between contact points and the distance where the wave can be considered as a plane wave plays an important role in the selection of the RVE height. A convergence analysis has also been performed to assure that the element size near the surfaces can capture the plastic deformation near the surface. It has been observed that the plastic deformation is more localized for the case with smaller elements and also that the maximum effective plastic strain rate values are higher. As expected, the transverse velocity is directly affected by this effect. Convergence is obtained for element sizes less than 1 μm. The analyst should keep this in mind not only to have a good resolution of the surface roughness, but also to properly capture the plastic deformation and its temperature dependence near the contact region.

Fig. 5(a) shows the evolution of stress and microcrack pattern due to the frictional sliding between the ceramic and steel target. Cracks nucleate at the ceramic surface and propagate through the ceramic. Friction and surface roughness are the principal sources

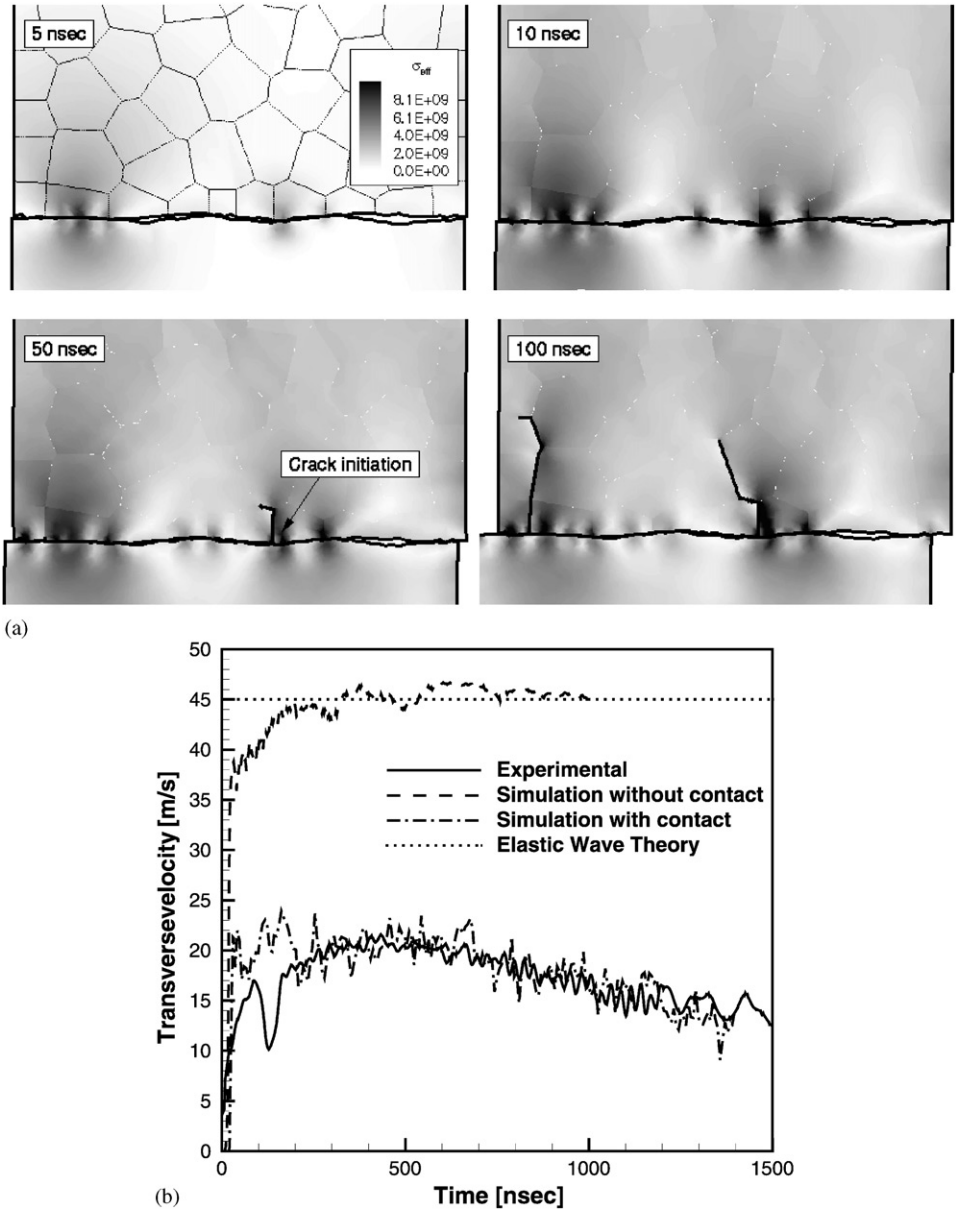


Fig. 5. (a) Evolution of effective stress on both ceramic and steel target plates. Microcracks are initiated at the surface and propagate through the ceramic. (b) Comparison between experimental result, numerical simulation without considering contact between ceramic and target plates, and simulation including contact and surface roughness between ceramic and target plates.

of crack nucleation. Temperature increases of 300°K above room temperature are generated according to this model. Fig. 5(b) shows a comparison between experimental data and the new numerical simulations considering contact and surface roughness between the ceramic and target. In the same figure, the transverse velocity obtained from previous simulations, without considering frictional sliding, are also included. The new numerical simulations are capable of capturing the transverse velocity of about 20 m/s, while the simulations including microcracking but omitting frictional effects result in a transverse velocity of about 45 m/s (Zavattieri et al., 2001). This transverse velocity reaches the level predicted assuming elastic response of the materials and absence of sliding.

Another important phenomenon observed in the experiment and in these new numerical simulations is the progressive reduction of the transverse velocity after 500 ns. Fig. 6 shows clearly how the surface of the steel target is deformed as the ceramic slides. The reduction of the transverse velocity can be attributed to the decrease of resistance that the steel offers to the ceramic as its sub-surface deforms. Sliding between the ceramic and steel surfaces is facilitated by plastic deformation of the steel surface, which gets flatter.

It is somewhat surprising and unexpected that these preliminary calculations can predict the physics of the recorded transverse velocity. The reader should note that by using experimentally measured roughness parameters and a well-established set of parameters for the hampden steel plate, the model is able to predict the main features observed experimentally. As previously mentioned, ceramic damage in the form of microcracking could not predict the reduction in transverse velocity as measured in the experiments. We examine some additional features related to inelastic mechanisms in later sections.

### 3.1. Effect of surface roughness parameters

In order to study the effect of surface roughness in the ceramic and steel target plates, five different meshes have been used. Fig. 7 shows the interfaces for these five meshes. Keeping the same values of "*peaks*" and "*valleys*", three different values of the wave length $\lambda$ have been used for each case. The resulting values of $R_a$ and RMS are similar for all the cases. Meshes A, B and C correspond to the same surface properties of the steel and different roughness for the ceramic with $\lambda$ decreasing from A to C. Meshes B, D and E have been used to study the effect of surface roughness in the steel keeping the same surface properties for the ceramic.

The numerical simulation shown in Fig. 5(b) has been performed using mesh B ($\lambda = 15$ μm). In all these calculations a high value of the hardening exponent ($\beta = 1000$) has been considered. Figs. 8(a) and (b) show the effect of surface roughness parameters on the transverse velocity. In all cases, the larger the value of $\lambda$, the larger the transverse velocity. It is observed that this effect is more important for the ceramic. Some interesting features are observed in the transverse velocity histories. To understand further the sources of these features, the contact area and effective friction coefficient are plotted in Figs. 8(c)–(f). It should be noted that no friction is considered in the contact algorithm ($\mu = 0$, see Espinosa et al., 1998b); in other words, the frictional

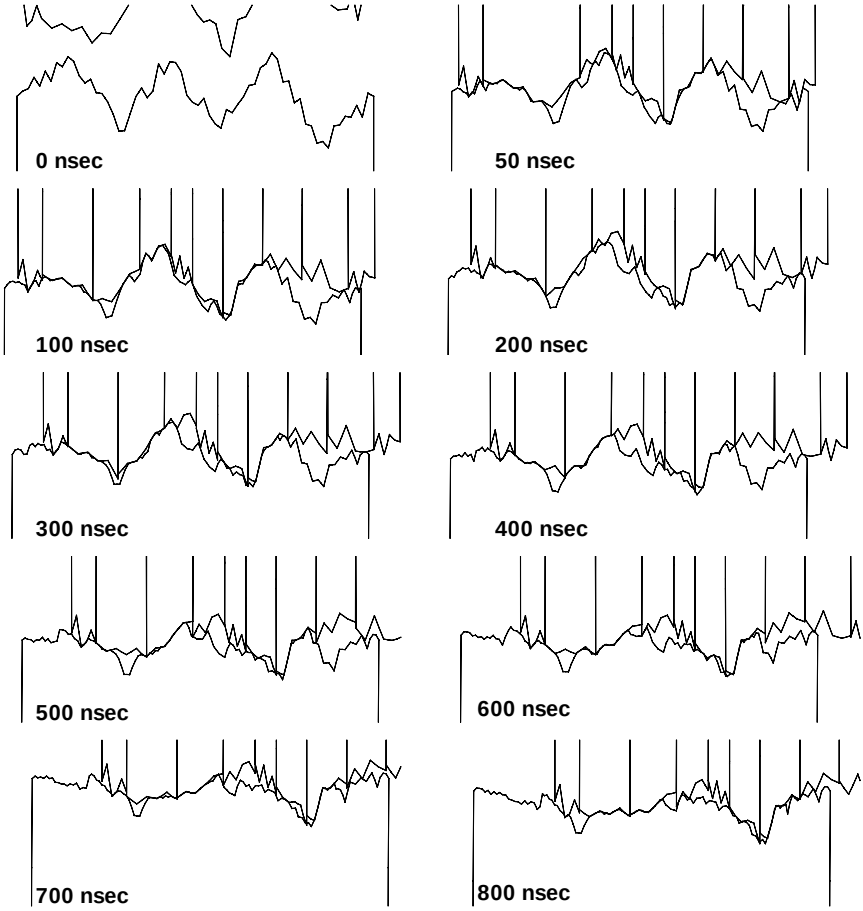


Fig. 6. Deformation of steel surface. This sequence shows clearly how the surface of the steel target deforms as the ceramic plate slides. Vertical lines above the ceramic surface denote grain boundaries. It should be noted that the figure is not at scale and all real angles are different as they are seen in this figure.

phenomenon is modeled explicitly. For these cases, the effective friction coefficient is taken from the ratio $\mu_{\text{eff}} = \tau/\sigma_{\text{n}}$.

From these analyses, it can be concluded that the surface roughness of the different materials plays an important role in the transverse velocity history observed at the bottom of the target plate. Friction coefficient histories ranging from progressive increase (hardening) to progressive decrease (softening) can be obtained as a function of surface characteristics, for the same pair of materials. Since transverse and normal velocity histories are the only real-time experimental information obtained from the material behavior during the deformation process, it is very difficult to gain a full understanding of the failure mechanisms only by these means. Pressure–shear experiments do not provide direct quantitative information on crack density, grain plasticity or twinning

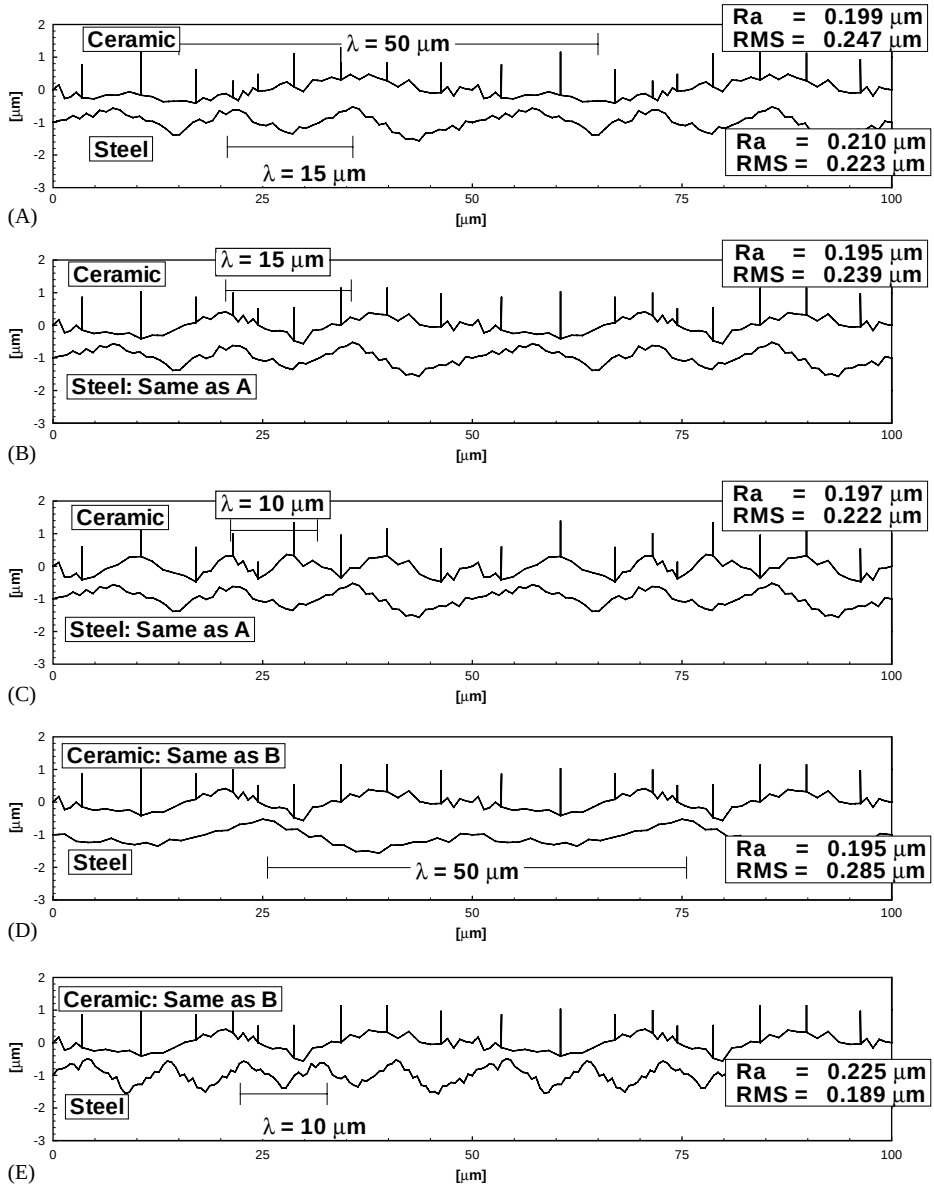


Fig. 7. Five different meshes have been used to study the effect of surface roughness in the ceramic and steel target plates. For each case, different values of the wavelength, $\lambda$, have been used in the ceramic and target. Vertical lines in the ceramic correspond to grain boundaries.

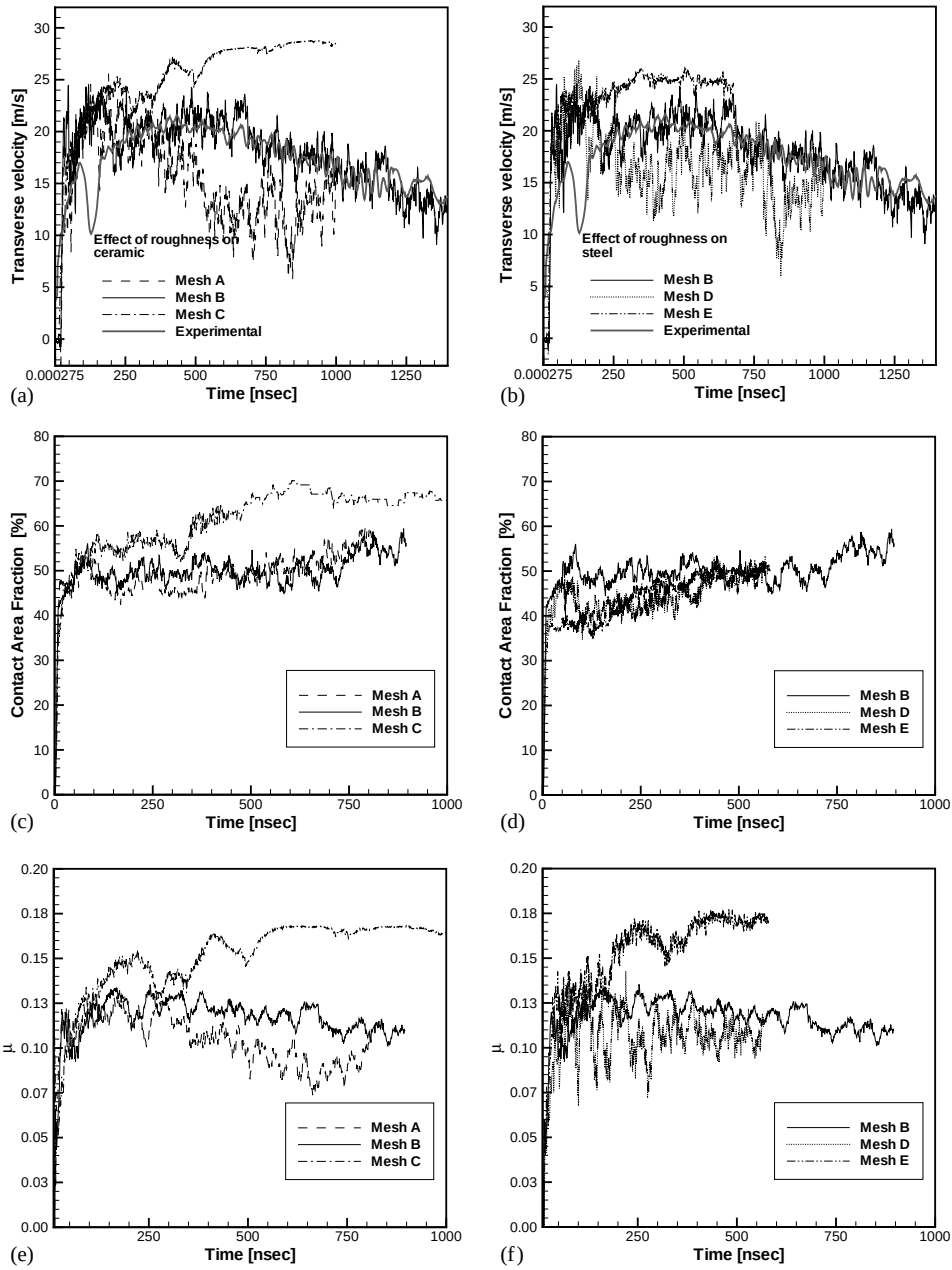


Fig. 8. Effect of surface roughness: (a) and (b) on the transverse velocity; (c) and (d) on the effective contact area (the ceramic is in full contact with the target when the effective contact area is equal to 100%); (e) and (f) on the effective friction coefficient.

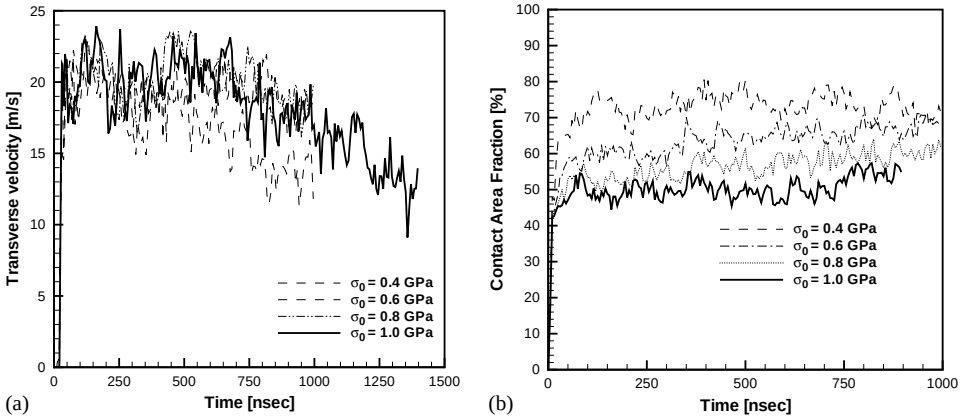


Fig. 9. Effect of steel initial yield stress: (a) on the transverse velocity; and (b) on the effective contact area.

and its rate of change as a function of applied deformation rate. Numerical simulations based on our knowledge of the material and its surfaces are required. It should be noted that a new methodology for testing and modeling frictional phenomena is presented in this work. With this new computational/experimental technique frictional mechanisms at brittle–ductile interfaces, as well as brittle–brittle or ductile–ductile interfaces can be examined in detail.

### 3.2. Effect of bulk material properties

It is clear that an in-depth analysis of the effect of the behavior of both materials is needed in order to fully identify *all* inelasticity and damage sources responsible for the measured experimental results. Whether the observed transverse velocity history is due to surface, bulk material properties or both can only be assessed through a sensitivity analysis of the steel anvils and ceramic specimen. In this section a systematic study of the main material properties of the anvil plates is carried out to investigate the role of the steel material in the transverse velocity.

#### 3.2.1. Effect of steel initial yield stress

The effect of the steel initial yield stress, $\sigma_0$, is studied with the aid of Mesh B. The transverse velocity is shown in Fig. 9(a). The transverse velocity decays faster for lower values of $\sigma_0$, but it does not affect the normal velocity history. The effect of $\sigma_0$ on the effective contact is shown in Fig. 9(b). The effective contact area increases appreciably as the steel initial yield stress decreases. This is consistent with more pronounced plastic deformation in the steel plate, which allows the material to deform and flow such that it maximizes the area of contact between both bodies. However, it has been found that the effective friction coefficient is not affected by $\sigma_0$.

Fig. 10 shows the spatial distribution of the effective plastic strain rate and temperature for different values of $\sigma_0$. These plots explain why the transverse velocity decreases

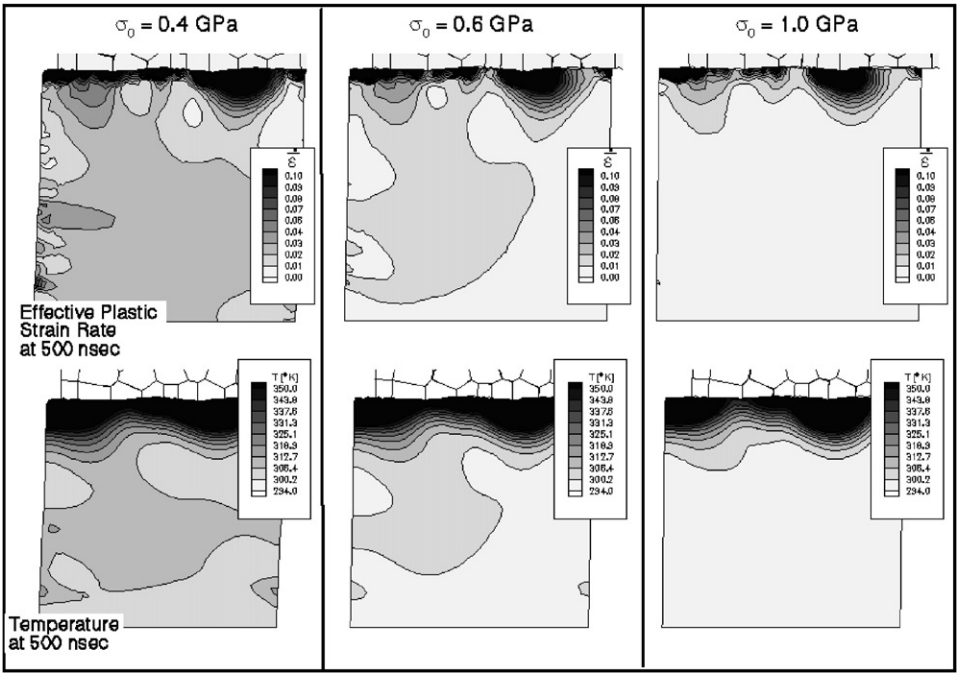


Fig. 10. Effect of steel initial yield stress on the spatial distribution of the effective plastic strain rate and temperature.

more rapidly for $\sigma_0 = 0.4$ GPa, while the effective contact area increases. Both, effective plastic strain rate and temperature, spread more into the steel plate as $\sigma_0$ decreases. Likewise, the capability for transferring the shear traction is reduced and this event is manifested in a decrease in transverse velocity. The large plastic deformation in the zone close to the surface maximizes the contact between the bodies but the reduction of shear stress controls the phenomenon.

### 3.2.2. *Effect of steel hardening exponent*

In the previous calculations, a high value of the hardening exponent was considered ($\beta = 1000$). The hardening effect is usually attributed to an increase in the stress needed to induce the motion of dislocations after the material has accumulated large plastic strains. On the surface, this phenomenon is altered due to the presence of the surface. If the plastic deformation is localized only near the surface, dislocations in the sub-surface can move towards the surface with more probability to be eliminated by image dislocations. Since all the plastic deformation in these simulations is localized in a region near the free surface of the steel target, it is reasonable to assume low hardening effects in the visco-plastic model. In this section the effect of hardening is examined for typical values of the hardening exponent (i.e. $\beta = 5$, 10, 50, etc.).

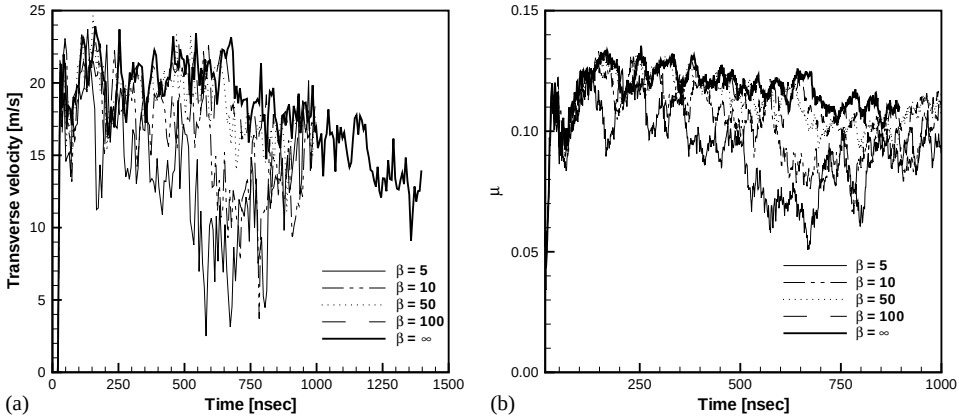


Fig. 11. Effect of steel hardening exponent: (a) on the transverse velocity; and (b) on the effective friction coefficient.

Fig. 11(a) shows the effect of the hardening exponent on the transverse velocity. This plot clearly shows an increase in velocity decay for those cases with low values of $\beta$ (high hardening). Unlike the case with a low yield stress, where a similar behavior was observed, no plastic deformation is localized in the target near the contact surface. As in the previous analysis, the normal velocity history is not affected by the hardening exponent. Fig. 11(b) show the effect of hardening on the effective friction coefficient. Unlike the case with low initial yield stress, the evolution of the effective contact area is similar for all five cases. However, the effective friction coefficient exhibits noticeable differences resulting in a lower value of $\mu_{\text{eff}}$ for smaller values of $\beta$. Likewise, the rate in effective friction coefficient reduction is quite different for each case. Compared with the steel target, no significant inelastic deformation is observed in the ceramic surface. This can be explained by the fact that the plastic deformation is diffused through the steel plate instead of being localized at the peaks as in the case with $\sigma_0 = 1$ GPa. As one would expect, the ceramic deforms more at high values of $\sigma_0$ or low values of $\beta$.

### 3.2.3. Effect of ceramic fracture properties

In this section the damage parameters characterizing the ceramic response are evaluated to study the effect of the bulk ceramic behavior on the measured velocity histories. For such purpose, three different grain boundary strengths ($T_{\max}$) have been considered ($T_{\max} = 0.1$, 1 and 10 GPa). In all cases $K_{\text{IC}} = 1.7$ MPa$\sqrt{m}$ is used.

Fig. 12 shows the transverse velocity and crack pattern for the three different values of $T_{\max}$. It is observed that the normal and transverse velocities are not highly affected by the parameters of the interface elements within the choice of the steel model parameters. The microcrack pattern after 1 μs is also shown in the figure. Although it is clear that the ceramic with a grain boundary strength of $T_{\max} = 0.1$ GPa shows much more damage than when $T_{\max} = 10$ GPa, the difference in the transverse velocity is negligible compared with the effect of any other parameter related

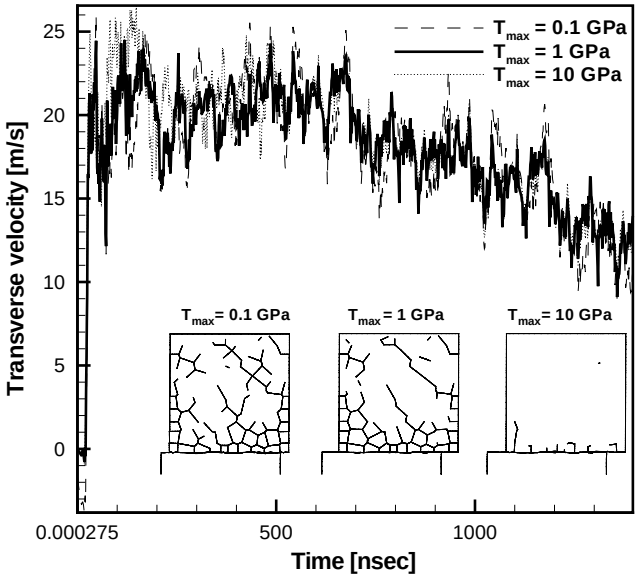


Fig. 12. Effect of ceramic strength, $T_{max}$, on the transverse velocity history.

to the frictional sliding. The implication is that the transverse velocity is dominated by the interface behavior rather than by the amount of ceramic damage. This counterintuitive effect can be explained by the fact that ceramic grains are highly confined with no empty volume to accommodate any significant relative motion between fragments. A completely different behavior would be expected in the case of highly porous ceramics.

## 4. Full-scale simulation

Full-scale simulations considering all of the key factors previously examined were carried out. Frictional sliding, surface roughness, intergranular microcracking, plasticity and heat generation in the flyer and target, and gap between specimen and flyer have been included. Fig. 13 shows a schematics of the finite element mesh generated taking into account target, flyer and specimen plates. The schematics of the boundary conditions is given in Fig. 3. For this analysis a grain size of 2 μm was considered and all the actual dimensions of the experiment were used (Espinosa et al., 2000b). The thickness of the specimen is 540 μm and the width of the RVE is 100 μm. The gap between flyer and specimen was also incorporated in the calculations. The roughness of the target, flyer and specimen are the same of those used in mesh B of Fig. 7, i.e., $R_a = 0.20$ μm, RMS $= 0.24$ μm and $\lambda = 15$ μm. The material parameters used in these simulations are specified in Tables 1–3.

As discussed by Espinosa and Zavattieri (2002b), Zavattieri and Espinosa (2001) and Zavattieri et al. (2001), it is physically incorrect to select a uniform $T_{max}$ and $K_{IC}$ for

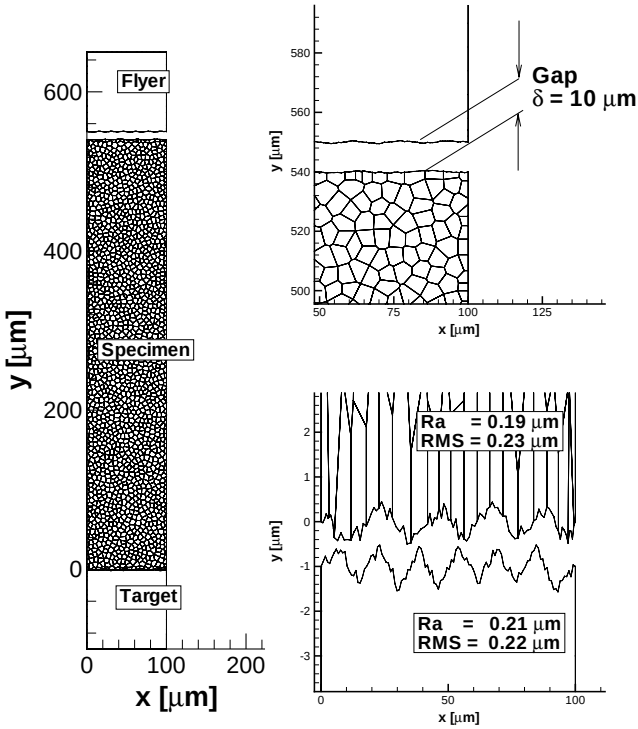


Fig. 13. Mesh with average grain size of 2 μm and surface roughness for full scale pressure–shear simulation.

all grain facets. Not only grain misorientation affects interfacial strength, but also the presence of glassy phase, glass pockets, and other impurities modify the ceramic grain boundary properties. Their random distribution leads to the consideration of a statistical variation in the interfacial strength dependent on grain misorientation and the presence of second phases. In the following analyses, the interfacial strength parameters will be described by a *Weibull* distribution. For instance the Weibull distribution for the maximum strength is given by

$$f(T_{\max}) = \frac{m(T_{\max})^{m-1}}{T_{\max^0}^{m}} \exp\left[-\left(\frac{T_{\max}}{T_{\max}^{0}}\right)^{m}\right], \quad T_{\max} > 0.$$

A similar expression is used for the Weibull distribution for the fracture toughness $K_{\mathrm{IC}}$. The Weibull parameters used in the simulations are $T_{\max}^{0} = 5$ GPa, $K_{\mathrm{IC}}^{0} = 1.7\ \mathrm{MPa} \cdot m^{1/2}$ and $m = 3$. These values have been independently identified for a similar ceramic by Zavattieri and Espinosa (2001).

One more detail has to be taken into consideration to simulate the real experiment. As was discussed in reference to Fig. 1, the normal and transverse particle velocities show a velocity reduction after an initial jump indicating the presence of a small gap between the $Al_2O_3/SiC$ nanocomposite and the multi-plate flyer. To determine the gap between the flyer and the specimen, an analysis based only on elastic wave theory was

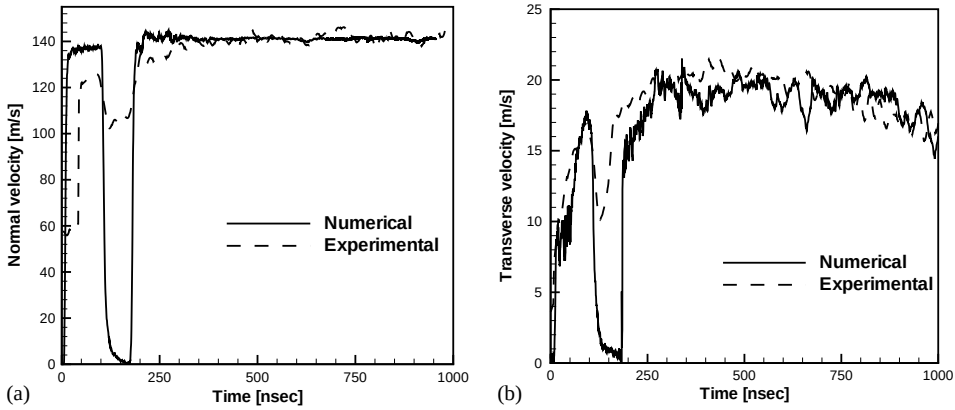


Fig. 14. Comparison of velocity histories obtained from full scale simulation and experiment: (a) normal velocity history; (b) transverse velocity history.

performed and compared with the experimental result. According to the duration of these pulses and the material parameters, a gap of approximately 10 μm was identified and used in the simulations.

### 4.1. Numerical results

Fig. 14 shows the normal and transverse velocity histories as they compared with the experimental data. In this simulation, there is complete unloading until the gap between flyer and specimen closes. This is not observed in the experimental trace likely due to the fact that in the real experiment there is a small but non-zero tilt between the flyer and the specimen. Our modeling does not account for this effect. Since this feature does not play any significant role nor it changes the subsequently recorded velocity histories, we ignore it. Examination of Fig. 14 clearly shows that both normal and transverse velocity histories, numerically obtained, are in good agreement with the experimental data. In particular, the transverse velocity history captures the peak value of about 20 m/s and the decay rate afterward.

Fig. 15 shows the crack evolution and pattern during the first microsecond. Microcracks initiate and propagate from the contact regions through the ceramic specimen. As the wave front advances, crack nucleation and growth occur up to the moment when the wave reaches the bottom face. A higher density of cracks is observed on the ceramic–steel interfaces and most of the microcracking in the bulk of the ceramic remains diluted.

## 5. Conclusions

In this paper a grain-level micromechanical model is introduced and used to identify failure mechanisms in pressure–shear experiments performed in brittle materials.

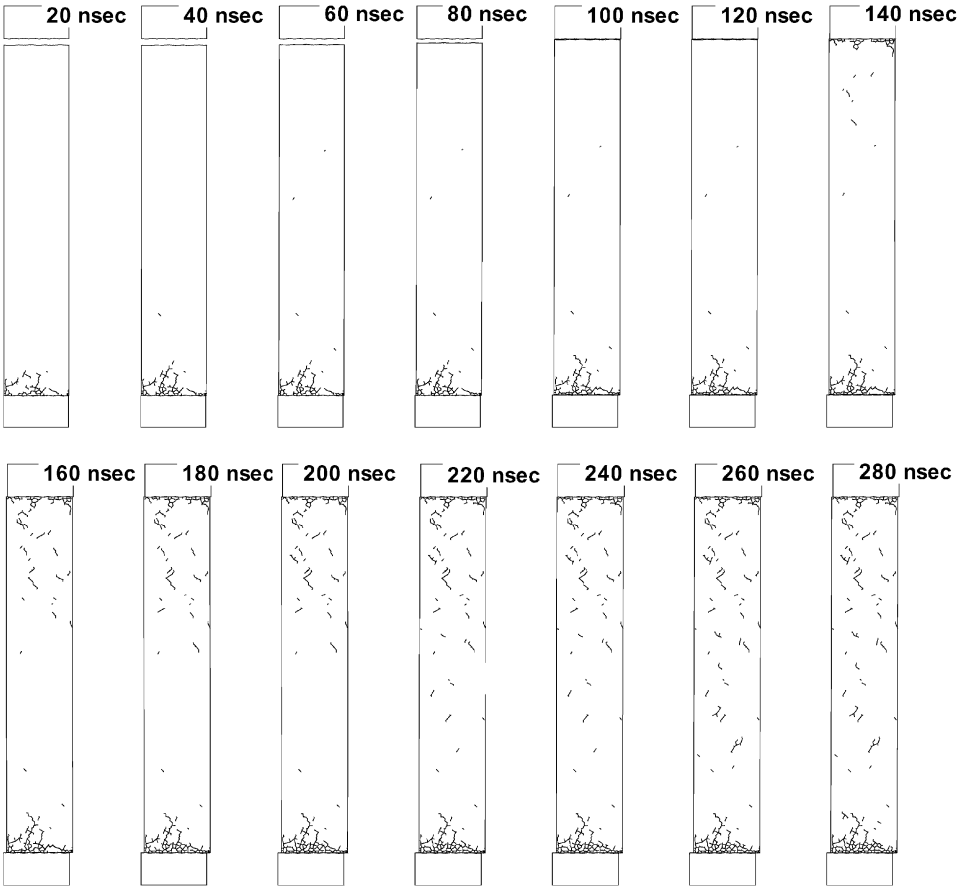


Fig. 15. Microcrack pattern in the ceramic specimen obtained from the full scale simulation.

The numerical results are discussed in terms of frictional effects, microcracking and viscoplasticity in relation to recorded velocity histories.

Two-dimensional simulations performed in this work and by Zavattieri et al. (2001) demonstrate that pressure–shear plate impact velocity profiles do not attenuate significantly even when accumulated damage within the specimen has extreme values. Although crack density and their patterns change from an almost intact ceramic to a completely cracked ceramic, changes in normal and transverse velocity histories, with respect to elastic predictions, are very subtle. This finding shows that identification of *bulk* properties in ceramics remains a very difficult problem. With advances in the synthesis of diamond and other ultra-hard materials, the possibility of designing configurations in which the flyer and target plates remain elastic, not only in the bulk but also at the surfaces, appears feasible. None of the pressure–shear experiments performed on hard brittle materials, which are reported in the literature, seems to meet this very demanding requirement. Therefore, based on the findings presented here, one can

conclude that surface effects are dominant and responsible for the observed attenuation from elastic predictions.

As mentioned in early work, ceramics are so susceptible to fragmentation, because of their low toughness, that they represent the most difficult materials to be investigated in wave propagation experiments with specimen recovery. Nonetheless, the simulations presented here show that our computational methodology is very valuable in the identification of dominant failure modes and in particular in the study of dynamic friction of hard brittle materials.

In this study, it has been observed that the normal velocity does not change from its theoretical value, obtained from elastic wave theory, even when contact and frictional sliding between bodies is considered. It has also been demonstrated that the transverse velocity history is highly dependent on the frictional sliding between the specimen and the target and that the phenomenon is highly sensitive to three key features: (1) plastic behavior of the softer material, steel target in this work, (2) surface roughness of both materials, and (3) applied pressure. None of these factors are directly related to the bulk inelastic behavior of the brittle specimen being tested.

Since the velocity histories taken from the back of the target are the only information available to the analyst, it can be concluded that pressure–shear experimental records, per se, are not sufficient to determine the mechanical behavior of brittle materials. However, when the experiments are analyzed by our grain level stochastic model, fundamental insight into dominant failure mechanisms, damage and inelasticity temporal and spatial distribution are obtained.

Our micromechanical model can be used to simulate the pressure–shear configuration for different impact velocities and angles, such that a relationship between crack density evolution and state of stress, temperature and initial damage is obtained. In this way, bridging between length scales can be accomplished not only to micromechanically characterize different brittle materials but also to use this information to refine theoretical formulations such as the multiple-plane microcracking model proposed by Espinosa (1995). Likewise, other frictional configurations can be modeled using the computational framework presented in this paper.

Another application that can take full advantage of our grain level model is the investigation of friction and reliability of microelectromechanical systems (MEMS). Friction and wear is the dominant failure mode in applications such as the Sandia microengine, Tanner et al. (1998).

## Acknowledgements

The authors acknowledge ARO and DoD HPCMP for providing supercomputer time on the 128 processors Origin 2000 at the Naval Research Laboratory—DC (NRL-DC). This research was supported by the National Science Foundation through Career Award Nos. CMS 9523113, CMS-9624364, the Office of Naval Research YIP through Award No. N00014-97-1-0550, the Army Research Office through ARO-MURI Award No. DAAH04-96-1-0331 and the Air Force Office of Scientific Research through Award No. F49620-98-1-0039.

## References

Buscaglia, G., Dari, E., 1997. Anisotropic mesh optimization and its applications in adaptivity. Int. J. Numer. Methods Eng. 40, 4119–4136.

Buscaglia, G., Dari, E., Zavattieri, P., 1997. Mesh optimization: some results in 3d elasticity. Élasticité, Viscoélasticité; et Contrôle Optimal ESAIM: Proceedings Lyon, France, pp. 1–16.

Camacho, G., Ortiz, M., 1996a. Adaptive Lagrangian modelling of ballistic penetration of metallic targets. Comput. Methods Appl. Mech. Eng. 142, 269–301.

Camacho, G.T., Ortiz, M., 1996b. Computational modeling of impact damage in brittle materials. Int. J. Solids Struct. 33, 2899–2938.

Clifton, R., Klopp, R., 1985. Pressure-shear plate impact testing. In: ASM Metal Handbook, Vol. 8, 9th Edition, American Society of Metals, Materials Park, OH, pp. 230–238.

Curran, D., Seaman, L., Cooper, T., Shockey, D., 1990. Micromechanical model for communication and granular flow of brittle material under high strain rate application to penetration of ceramic targets. Int. J. Impact Eng. 13, 53–83.

Espinosa, H., 1992. Micromechanics of the dynamic response of ceramics and ceramic composites. Ph.D. Thesis, Brown University, Providence, RI.

Espinosa, H., 1995. On the dynamic shear resistance of ceramic composites and its dependence on applied multiaxial deformation. Int. J. Solids Struct. 32, 3105.

Espinosa, H., Nemat-Nasser, S., 2000. Low velocity impact experiments. In: Lampan, S. (Ed.), Handbook, Vol. 8. ASM International, Metals Park.

Espinosa, H., Zavattieri, P., 2002a. A grain level model for the study of failure initiation and evolution in polycrystalline brittle materials, Part I: theory and numerical implementation. Mech. Mater., in press.

Espinosa, H., Zavattieri, P., 2002b. A grain level model for the study of dynamic failure initiation and evolution in polycrystalline brittle materials, Part II: numerical examples. Mech. Mater., in press.

Espinosa, H., Raiser, G., Clifton, R., Ortiz, M., 1992. Experimental observations and numerical modeling of inelasticity in dynamically loaded ceramics. J. Hard Mater. 3, 285–313.

Espinosa, H., Mello, M., Xu, Y., 1997. A variable sensitivity displacement interferometer with application to wave propagation experiments. J. Appl. Mech. 64, 123–131.

Espinosa, H., Zavattieri, P., Dwivedi, S., 1998a. A finite deformation continuum/discrete model for the description of fragmentation and damage in brittle materials. J. Mech. Phys. Solids 46 (10), 1909–1942.

Espinosa, H., Zavattieri, P., Emore, G., 1998b. Adaptive FEM computation of geometric and material nonlinearities with application to brittle failure. Mech. Mater. 29, 275–305.

Espinosa, H., Dwivedi, S., Lu, H.-C., 2000a. Modeling impact induced delamination of woven fiber reinforced composites with contact/cohesive laws. Comput. Methods Appl. Mech. Eng. 189, 259–290.

Espinosa, H., Patanella, A., Xu, Y., 2000b. Dynamic compression-shear response of brittle materials with specimen recovery. Exp. Mech. 40 (3), 321–330.

Espinosa, H., Lu, H.-C., Zavattieri, P., Dwivedi, S., 2001. A 3-d finite deformation anisotropic visco-plasticity model for fiber composites. J. Compos. Mater. 35 (5), 369–410.

Hearmon, R., 1956. The elastic constants of anisotropic materials ii. Adv. Phys. 5, 323–382.

Machcha, A., Nemat-Nasser, S., 1994. Pressure-shear recovery experiments. Mech. Mater. 18, 49–53.

Ortiz, M., Pandolfi, A., 1999. Finite-deformation irreversible cohesive elements for three-dimensional crack-propagation analysis. Int. J. Numer. Methods Eng. 44 (9), 1267–1282.

Raiser, G., 1993. Dynamic failure resistance of ceramics and glasses. Ph.D. Thesis, Brown University, Providence, RI.

Raiser, G., Clifton, R., Ortiz, M., 1990. A soft-recovery plate impact experiment for studying microcracking in ceramics. Mech. Mater. 10, 43–58.

Raiser, G., Wise, J., Clifton, R., Grady, D., Cox, D., 1994. Plate impact response of ceramics and glasses. J. Appl. Phys. 75 (8), 3862–3869.

Tanner, D., Peterson, K., Irwin, L., Tangyunyong, P., Miller, W., Eaton, W., Smith, N., Rodgers, S., 1998. Linkage design effect on the reliability of surface micromachined microengines driving a load. Proceedings of SPIE, Micromachining and Microfabrication Symposium, Vol. 3512, Santa Clara, CA, pp. 225–226.

Taylor, L., Flanagan, D., 1987. Pronto 2d: a two dimensional transient solid dynamics program. Sandia Report SAND86.

Tvergaard, V., 1990. Effect of fibre debonding in a whisker-reinforced material. Mater. Sci. Eng. A 125, 203.

Xu, X.-P., Needleman, A., 1995. Numerical simulation of dynamic interfacial crack growth allowing for crack growth away from the bond line. Int. J. Fract. 74, 253–275.

Yadav, S., Davis, J., Ramesh, K., 1993. Damage and recovery experiments using pressure-shear plate impact. In: Experimental Techniques in the Dynamics of Deformable Solids. American Society of Mechanical Engineers, Applied Mechanics Division, AMD, NY, USA, Vol. 165, pp. 71–78.

Zavattieri, P., Espinosa, H., 2001. Grain level model analysis of crack initiation and propagation in brittle materials. Acta Mater. 49, 4291–4311.

Zavattieri, P., Buscaglia, G., Dari, E., 1996a. Finite element mesh optimization in three dimensions. Latin Amer. Appl. Res. 26, 233–236.

Zavattieri, P., Dari, E.A., Buscaglia, G., 1996b. Optimization strategies in unstructured mesh generation. Int. J. Numer. Methods Eng. 39, 2055–2071.

Zavattieri, P., Raghuram, P., Espinosa, H., 2001. A computational model of ceramic microstructures subjected to multi-axial dynamic loading. J. Mech. Phys. Solids 49 (1), 27–68.

Zhou, M., Needleman, A., Clifton, R., 1994. Finite element simulations of shear localization in plate impact. J. Mech. Phys. Solids 42 (3), 423–458.